Fabrication and Characterization of Rare-Earth-Doped Nanostructures on Surfaces

Thomas J. Mullen,[†] Ming Zhang,[†] Wei Feng,[‡] Rita J. El-khouri,[†] Ling-Dong Sun,[‡] Chun-Hua Yan,[‡] Timothy E. Patten,[†] and Gang-yu Liu*,[†]

[†]Department of Chemistry, University of California, Davis, California 95616, United States, and [‡]Beijing National Laboratory for Molecular Sciences, State Key Lab of Rare Earth Materials Chemistry and Applications, PKU-HKU Joint Laboratory in Rare Earth Materials and Bioinorganic Chemistry, Peking University, Beijing, 100871, P. R. China

ABSTRACT This article presents a simple and practical means to produce rare-earth-based nanostructures, as well as a combined characterization of structure and optical properties *in situ*. A nanosphere lithography strategy combined with surface chemistry enables the production of arrays of β-$NaYF_4$:Yb,Er nanorings inlaid in an octadecyltrichlorosilane matrix. These arrays of nanorings are produced over the entire support, such as a 1 cm^2 glass coverslip. The dimension of nanorings can be varied by changing the deposition conditions. A home-constructed, multifunctional microscope integrating atomic force microscopy, near-field scanning optical microscopy, and far-field optical microscopy and spectroscopy is utilized to characterize the nanostructures. This *in situ* and combined characterization is important for rare-earth-containing nanomaterials in order to correlate local structure with upconversion photoluminescence. Knowledge gained from the investigation should facilitate materials design and optimization, for instance, in the context of photovoltaic devices and biofluorescent probes.

KEYWORDS: Rare-earth-doped · nanocrystal · nanosphere lithography · upconversion luminescence · near-field scanning optical microscopy · atomic force microscopy

Rare-earth-doped nanocrystals (RENs) have been proposed for a variety of applications including solid state lasers,[1] displays,[2,3] low-intensity IR imaging,[4] watermarking technology,[5] 3D storage media,[6] solar cells and other PV devices,[7−10] and biological probes.[11−14] Interest in these nanomaterials arises from their photoluminescent characteristic of upconversion whereby near-infrared radiation is absorbed followed by the subsequent emission of visible photons.[15−17] Additional advantages due to miniaturization to the nanoscale include increased surface area, faster speed, and smaller device size. In order to realize technological applications, strategies must be developed to integrate RENs as device components.

Composite REN nanostructures are of particular interest for applications in photovoltaic devices, displays, anticounterfeiting, and biological probes. However, particular advancements are required in order to facilitate their integration into technological devices. For photovoltaic devices or displays, large and ordered arrays of nanometer-scale surface structures are often desired in order to integrate various components.[8,10,18,19] In photovoltaic configuration, nanometer scale precision is important to minimize the path length of excitations in solar cell applications and to enable control and regulation of energy transfer between the RENs and photoconversion components. For displays, nanometer scale pixels will result in higher resolution and pixel density. These pixels must be in ordered arrays for high quality and addressable displays. For watermarking and anticounterfeiting substrates, the ability to generate thin and complex nanostructures will provide for enhanced security features.[5] For biosensitive probe substrates, regular and ordered nanoscale arrays enable reproducibility and a larger dynamic range.[13,20] Further, nanoscale structures will provide for and enable higher sensitivity and faster readouts for biosensitive probes. By developing methodologies to generate multicomponent RENs, the technological promise of these nanometer scale materials can be realized.

With all of these potential applications, there has been significant interest and several strategies reported toward generating multicomponent, composite REN nanostructures. For example, microcontact printing and the condensation of water droplets were combined to generate ordered microscale patterns of $NaYF_4$:Yb,Er nanorings.[21] This method produced patterns as small as $\sim 8\,\mu$m. Further miniaturization to the nanometer scale is difficult due to the stamp size in microcontact printing. Another patterning technique was demonstrated by

* Address correspondence to liu@chem.ucdavis.edu.

Received for review May 24, 2011 and accepted July 22, 2011.

Published online July 22, 2011
10.1021/nn201910f

© 2011 American Chemical Society

combining a micromolding in capillaries (MIMIC) strategy with polystyrene spheres to make 3-D nanoscale photonic crystals of $NaYF_4$:Yb,Er nanocrystals.[14] This approach produced 3-D nanoscale REN structures of a single component and over microscale areas.[22,23] High throughput and further addition of multicomponent structures are difficult due to the capillary forces required to assemble the polystyrene spheres. Multicomponent heterostructures composed of CdSe quantum dots and $NaYF_4$:Yb,Er nanocrystals were attempted by casting them into thin films between two electrodes.[24] When this film was exposed to IR light, excitons were generated *via* the upconversion by the RENs, which lead to a reversible IR photoconductivity switch. It is encouraging to observe RENs in an electronic device, although the nanostructures are randomly dispersed across the substrate without long-range order. Similar composite materials have been reported by mixing polymer films with RENs and then depositing them across a substrate.[5,25,26]

Given these precedents, we decided to investigate whether nanosphere lithography methods could be adapted to improve the technical requirements identified, that is, to produce large area, ordered nanostructures of RENs with controllable pattern dimensions and geometry. In this work, we report robust arrays of rare-earth nanostructures *via* a combination of a nanosphere lithography strategy and vapor deposition of organic siloxanes. This method reproducibly generates arrays of nanoscale rings composed of individual β-$NaYF_4$:Yb,Er nanocrystals within an octadecyltrichlorosilane (OTS) matrix.

RESULTS AND DISCUSSION

Fabrication of Arrays of Rare-Earth-Based Nanostructures *via* Nanosphere Lithography. Composite REN and organic surface supported nanostructures composed of arrays of β-$NaYF_4$:Yb,Er nanorings inlaid in an OTS monolayer were produced by the two strategies outlined in Figure 1. For both procedures, a 50 μL aliquot of a 3% solution by weight of 1 μm silica microspheres suspended in water was cast across a glass coverslip and allowed to dry in the ambient environment at room temperature (23 °C) for at least 1 h. These conditions yield close-packed silica spheres consistent with previous reports.[27−32] For the first strategy, which produced high-quality monolayer $NaYF_4$:Yb,Er nanorings, the substrate was placed into an oven overnight at 125 °C. A 50 μL aliquot of a 4 mg/mL solution of 22 nm β-$NaYF_4$:Yb,Er nanocrystals suspended in chloroform was deposited across the surface, covered with a watch glass, and allowed to dry for 1 h. As the solvent dried, the nanocrystals were pushed, *via* the interplay of capillary forces and adhesions forces between the substrate and nanocrystals, into the region between the silica microsphere and substrate.[33] By systematically varying the concentration, 4 mg/mL was determined to be the optimal condition with which to produce arrays of β-$NaYF_4$:Yb,Er nanorings with thicknesses of 1−2 layers of nanocrystals. The silica microspheres were removed from the glass coverslip by applying and peeling away a piece of transparent tape, and the remaining surface structures were subsequently characterized with the home-built microscope that combined atomic force microscopy (AFM), near-field scanning optical microscopy (NSOM), and far-field optical microscopy. Although this fabrication strategy produces high quality monolayers of REN nanorings for individual nanocrystal characterization, these samples are not mechanically stable for contact-mode AFM imaging because the nanocrystals are moved by the AFM tip during the scan. The second strategy produced more mechanically stable nanostructures by vapor depositing an OTS SAM on the substrate after the formation of

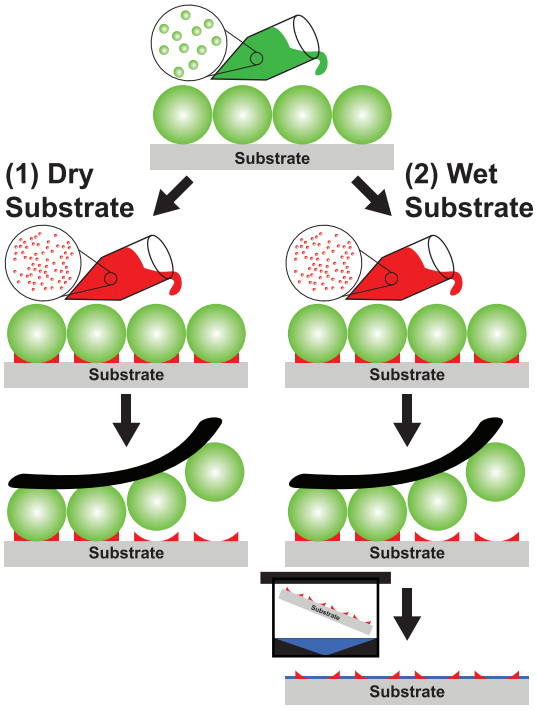

Figure 1. Fabrication of arrays of RENs and organic surface supported nanostructures *via* nanosphere lithography. Silica microspheres are cast across a glass coverslip and allowed to dry in the ambient environment for at least 1 h. *Wet Substrate*. The glass coverslip is placed into an oven overnight at 125 °C. A solution of β-$NaYF_4$:Yb,Er suspended in chloroform is cast across the glass coverslip, covered with a watch glass, and allowed to dry for at least 1 h. The silica microspheres are removed by applying and peeling off a piece of transparent tape leaving behind β-$NaYF_4$:Yb,Er nanorings. *Dry Substrate*. After the silica microsphere solution dries for 1 h in ambient, a solution of β-$NaYF_4$:Yb,Er suspended in chloroform is cast across the glass coverslip, covered with a watch glass, and allowed to dry for at least 1 h. The silica microspheres are removed by applying and peeling off a piece of transparent tape leaving behind β-$NaYF_4$:Yb,Er nanorings. The glass coverslip is placed into a container with OTS, sealed, and placed into an oven at 70 °C for 4 h generating the composite β-$NaYF_4$:Yb,Er nanorings within an OTS matrix.

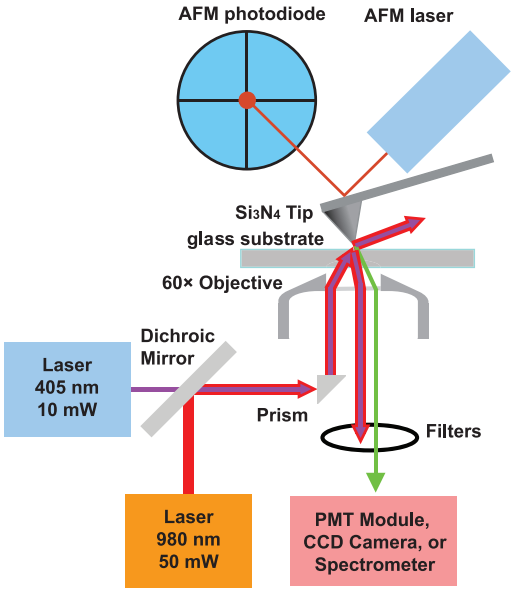

Figure 2. Schematic of a home-constructed microscope combining AFM, NSOM, and far-field optical microscopy.

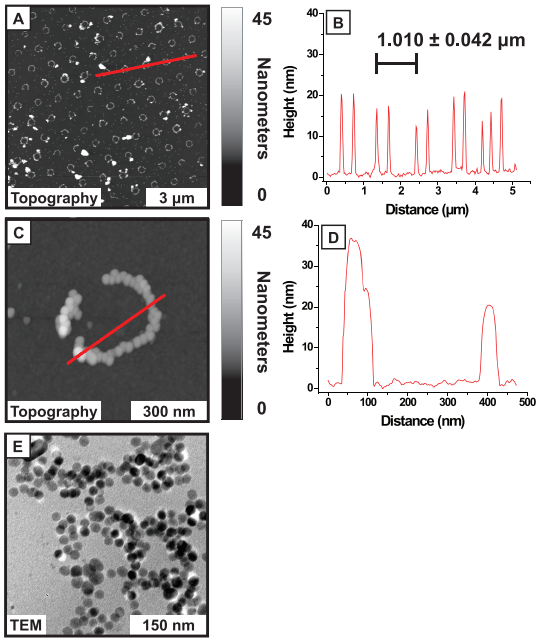

Figure 3. Arrays of β- $NaYF_4$:Yb,Er nanocrystals rings. (A) A 10 μm^2 topographic AFM image and (B) corresponding cursor profile of an array of β-$NaYF_4$:Yb,Er nanorings. (C) A 800 nm^2 topographic AFM image and (D) corresponding cursor profile of an individual β-$NaYF_4$:Yb,Er nanoring. Both AFM images were acquired in tapping mode using a Si AC240 cantilever. (E) TEM image of β-$NaYF_4$:Yb,Er nanocrystals.

the nanorings. Once the silica microspheres were deposited and allowed to dry in the ambient environment for 1 h, a 50 μL aliquot of a 4 mg/mL solution of 22 nm β-$NaYF_4$:Yb,Er nanocrystals suspended in chloroform was deposited across the surface, covered with a watch glass, and allowed to dry for at least 1 h. The silica microspheres were removed from the glass coverslip by applying and peeling away a piece of transparent tape. To generate the OTS monolayer *via* vapor deposition, 200 μL of OTS were pipetted into a container, and the glass substrate with the arrays of β-$NaYF_4$:Yb,Er nanorings was placed onto a support in the container to prevent contact with the neat OTS. The container was sealed, placed into an oven, and heated at 70 °C for at least 4 h under ambient pressure. This strategy produces OTS monolayers as per previous protocols.[29,31,32] By drying the substrate only in the ambient and not drying them in an oven, there is sufficient water present to initiate surface hydrosilylation of the OTS molecules as well as other organosilanes. The substrate was removed from the container and subsequently characterized with the home-built combined AFM, NSOM, and far-field microscope.

Multifunctional Imaging and Spectroscopy. To investigate and to compare the topographic and optical features of the nanostructures produced, an AFM microscope is modified to integrate apertureless NSOM,[34,35] AFM, and far-field optical microscopy and spectroscopy. Figure 2 shows the schematic of the instrumentation, and further details can be found in the Materials and Methods section. The optical path allows two laser lines: a 405 nm line for the excitation of Si_3N_4 tip in NSOM imaging, and a 980 nm line for measuring the upconversion luminescence of β-$NaYF_4$:Yb,Er nanorings. The beam is directed to and focused on the sample *via* a prism and a 60× bright field objective, respectively. The emission from the Si_3N_4 tip or RENs is collected by the same objective and passes through a series of filters to remove AFM laser intensity and excitation. The NSOM, farfield imaging and spectroscopy signals are then collected *via* a photomultiplier tube, CCD camera, and fiber optic spectrometer, respectively. This instrumentation enables high resolution AFM and NSOM imaging, in conjunction with far field optical viewing and spectroscopy, *in situ*.

Arrays of β-$NaYF_4$:Yb,Er Nanorings. Arrays of β-$NaYF_4$:Yb,Er nanorings were fabricated over the entire surface of glass coverslips. Figure 3A shows a representative AFM image of a 10 μm^2 region to reveal the arrays of β-$NaYF_4$:Yb,Er nanorings. Figure 3B shows a representative cursor profile across 5 nanorings as indicated by the red line in Figure 3A. These arrays of β-$NaYF_4$:Yb,Er nanorings are 17 ± 5 nm in height and follow a hexagonal symmetry. The periodicity measures 1.010 ± 0.041 μm, which is consistent with the 1 μm silica microspheres used as templates. Defects such as incomplete or missing rings, individual nanocrystals, and agglomerates of nanocrystals are observed throughout the arrays of β-$NaYF_4$:Yb,Er nanorings. Figure 3C shows a high-resolution AFM image of a typical ring composed of individual β-$NaYF_4$:Yb,Er nanocrystals. The outer and inner diameters, determined from cursor profiles, are 389.6 ± 18.8 and 276.5 ± 16.1 nm, respectively. This particular nanoring is composed of 60 individual β-$NaYF_4$:Yb,Er nanocrystals

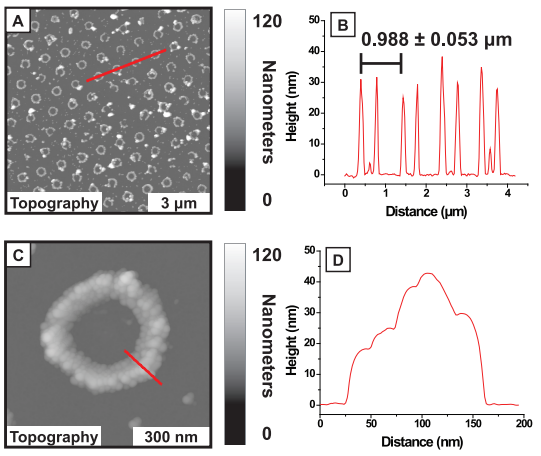

Figure 4. Composite nanoscale surface structures of arrays of β-$NaYF_4$:Yb,Er rings within an OTS monolayer. (A) A 10 μm^2 topographic AFM image and (B) corresponding cursor profile of an array of β-$NaYF_4$:Yb,Er nanorings in an OTS matrix. (C) A 800 nm^2 topographic AFM image and (D) corresponding cursor profile of an individual β-$NaYF_4$:Yb,Er nanoring in an OTS matrix. Both AFM images were acquired in tapping mode using a Si AC240 cantilever with a spring constant of 2.0 N/m.

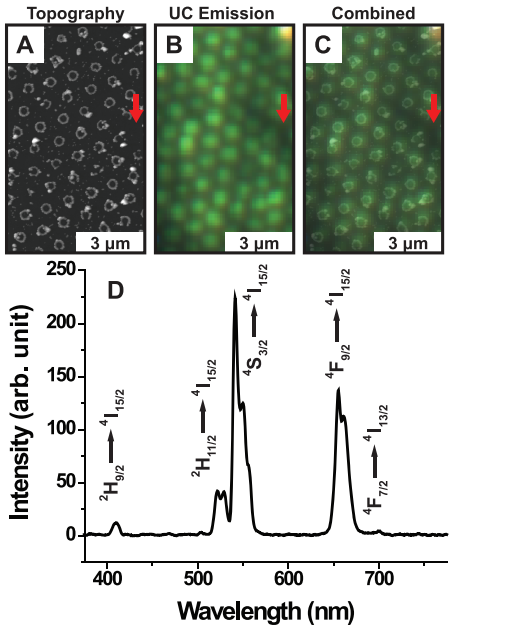

Figure 5. Correlation of AFM topographic features to upconversion luminescence. (A) Tapping-mode AFM and (B) upconversion luminescence images acquired sequentially over the same region of composite nanoscale surface structures of arrays of β-$NaYF_4$:Yb,Er nanorings within an OTS matrix. (C) Overlay of the AFM and upconversion luminescence images. (D) Upconversion luminescence spectra acquired over the same region after the upconversion luminescence image. The tapping-mode AFM image was acquired using a Si AC240 cantilever with a spring constant of 2.0 N/m. The image exposure time was 3 s, and the spectra exposure time was 15 s.

and is approximately 87% complete. The majority of the β-$NaYF_4$:Yb,Er nanoring is composed of a monolayer of nanocrystals; however, some regions are composed of bilayers of stacked nanocrystals. Figure 3D shows a representative cursor profile across the monolayer and bilayer regions of the β-$NaYF_4$:Yb,Er nanoring as indicated by the red line in Figure 3C. The nanocrystals in the monolayer region have a height of 19.2 nm, which is consistent with the particle size from TEM imaging of the same batch of β-$NaYF_4$:Yb,Er nanocrystals (Figure 3E). In the bilayer region, two vertical heights, 35.9 and 25.5 nm, are observed in the cursor profile suggesting that the bilayer region is composed of stacked nanocrystals. The height measured is less than atop stacking and consistent with particles stacking on the hollow sites of the base layer.

Arrays of β-$NaYF_4$:Yb,Er Nanorings Inlaid in an OTS SAM. Arrays of β-$NaYF_4$:Yb,Er nanorings inlaid in an OTS SAM were fabricated across the entire surface of glass coverslips. Figure 4A shows a representative AFM image of a 10 μm^2 region of arrays of β-$NaYF_4$:Yb,Er nanorings inlaid within an OTS SAM. A cursor profile across 4 nanorings is shown in Figure 4B. Nanorings follow a hexagonal arrangement with the periodicity of 0.99 $\pm$ 0.05 μm, which is consistent with the size of a 1 μm silica template. The majority of these nanorings are complete, with agglomerates, and lattice defects are randomly present. Further, the height of these nanorings measures 31 $\pm$ 9 nm. Figure 4C depicts a characteristic β-$NaYF_4$:Yb,Er nanoring inlaid in an OTS SAM. The size of individual β-$NaYF_4$:Yb,Er nanocrystals are consistent with that from *ex situ* TEM imaging (Figure 3E). The outer and inner diameter of this particular nanoring, as determined from 4 cursor profiles across the nanoring, are 469.5 $\pm$ 17.7 and 275.3 $\pm$ 15.9 nm, respectively. The nanoring has a lateral width of five closely packed nanoparticles, as measured from Figure 4D, which most likely results from stacking and packing of these nanocrystals. The height of this nanoring ranges from 17.6 nm, which is consistent with an individual nanocrystal, to 41.8 nm, which illustrates that the nanocrystals are stacked upon each other forming bilayer and multilayers.

Composite β-$NaYF_4$:Yb,Er Nanocrystal and OTS Nanostructures Retain Upconversion Properties. Using the home constructed, multiline instrumentation capable of sequential AFM and far-field microscopy and spectroscopy, the topographic features of the composite β-$NaYF_4$:Yb,Er nanocrystal and OTS surface supported nanostructures were correlated to the observed upconversion emission. Figure 5A and 5B show a tapping-mode AFM image and far-field optical image of upconversion luminescence, respectively, acquired sequentially over the same region. Figure 5C shows an overlay of the two images correlating the two channels. From the AFM image, rings composed of individual RENs as well as agglomerates are observed as described in the previous section. Upon excitation with a 980 nm laser, these features correlate to bright, homogeneous, green emission in the far-field optical image, which is attributed to

the upconversion luminescence of the β-$NaYF_4$:Yb,Er nanorings. Little to no optical intensity is observed in the regions containing lattice defects in the AFM image, as indicated by the red arrows. Similarly, the brightest intensity (top, right corner) corresponds to agglomerates of the β-$NaYF_4$:Yb,Er nanocrystals. Figure 5D shows the photoluminescent spectrum acquired in the same region after the far-field imaging. The five emission peaks observed are consistent with the known transitions reported for that suspended in solution.[36−38] For example, the strongest pair of green emission at 520 and 550 nm correspond to the $^2H_{11/2}\rightarrow{}^4I_{15/2}$ and $^4S_{3/2}\rightarrow{}^4I_{15/2}$, respectively. Similarly, the red emission band around 670 nm is ascribed to the $^4F_{9/2}\rightarrow{}^4I_{15/2}$ transition. The weak bands around 410 and 700 nm correspond to the $^2H_{9/2}\rightarrow{}^4I_{15/2}$ and $^4F_{7/2}\rightarrow{}^4I_{13/2}$ transitions, respectively. The upconversion characteristics of the β-$NaYF_4$:Yb,Er nanocrystals are retained in all nanostructures produced on surfaces. In other words, the upconversion emission of these nanomaterials is independent of the aggregation status. The independence of the upconversion emission from the aggregation state of the RENs is of particular interest for device applications because other nanomaterials, such as metal nanoparticles or semiconductor quantum dots, would exhibit strong dependence on aggregations in a solution phase and on a surface.

NSOM Characterization of Intraring Optical Property. Figure 6A and 6B show topographic and NSOM images acquired simultaneously of an array of β-$NaYF_4$:Yb,Er nanorings within an OTS monolayer. From the contact-mode AFM image, the lateral and vertical dimensions are consistent with the features observed in the tapping mode AFM images of the same substrate (Figure 4). Further, nanorings exhibit stability under contact scanning, with only loosely bound nanocrystals being swept away. Without an OTS matrix, nanorings show much less stability, with gradual depletion of the ring geometry, and streaks in the fast scan direction in AFM images. This observation further indicates the importance of OTS, in the improvement of the mechanical stability and integrity of the β-$NaYF_4$:Yb,Er nanorings. In the NSOM image, the dark contrast corresponds well with the topography of β-$NaYF_4$:Yb, Er nanorings. The inhomogeneity within nanorings is also visible in the NSOM image, indicating the sensitivity of NSOM to the packing of RENs. For instance, the darkest features are due to the stacking of nanocrystals. Combined cursor profiles of both topography (red) and NSOM optical (blue) channels are shown in Figure 6C over the same nanoring, to reveal the correlation quantitatively. The tallest feature (68 nm) in the AFM topograph correlates to the darkest contrast in the NSOM channel, as an agglomerate of β-$NaYF_4$:Yb,Er nanocrystals absorb more photons than monolayer regions. The shorter features in the AFM topography (38 nm) correspond well with the second

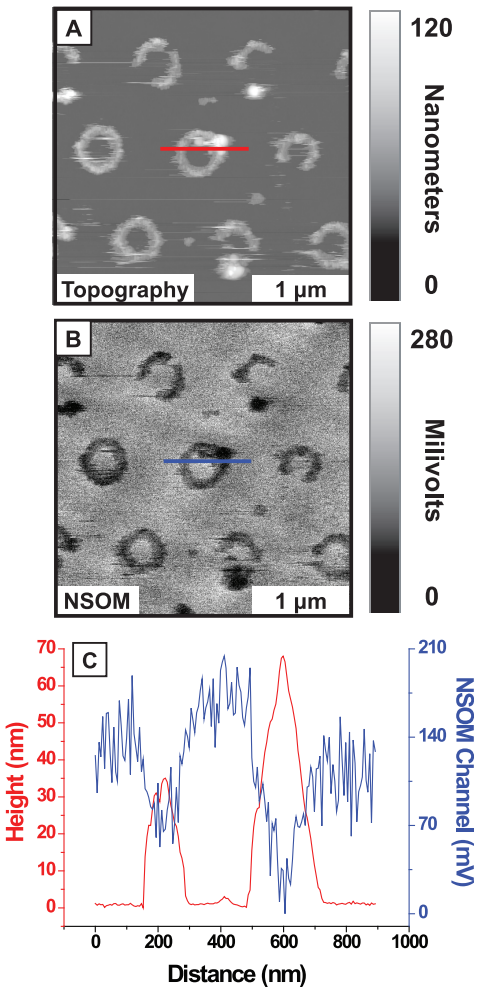

Figure 6. NSOM imaging of composite nanoscale surface structures of arrays of β-$NaYF_4$:Yb,Er rings within an OTS monolayer. (A) Topographic and (B) NSOM images of an array of β-$NaYF_4$:Yb,Er nanorings within an OTS matrix. (C) Corresponding cursor profiles for topography and NSOM channel. The AFM image was acquired in contact mode using a Si_3N_4 cantilever with a spring constant of 0.1 N/m.

darkest contrast in the NSOM image. Finally, OTS monolayer regions are optically transparent and, thus, manifest into the brightest contrast in the NSOM images. The sensitivity of NSOM contrast to the material type and particle packing shown in Figure 6 is encouraging, because it demonstrates the feasibility of attaining an optical signal and nanometer resolution under this setup. Work is in progress to tune the photoluminescent wavelength of the cantilever to better match the REN's absorption.

CONCLUSION

Arrays of ordered β-$NaYF_4$:Yb,Er nanorings inlaid in an OTS matrix were fabricated using nanosphere lithography and siloxane surface chemistry. Combined AFM, NSOM, and far-field microscopy and spectroscopy were utilized to characterize their structure in correlation to the photoluminescent properties at a single feature and single particle level. Nanorings with

outside diameters ranging from 389.6 to 469.5 nm were produced over the entire surface, e.g. 1 cm^2 glass coverslips. An advantage of this fabrication strategy is the simplicity and versatility of nanosphere lithography and siloxane chemistry, both of which can be routinely carried out on a benchtop in an ambient environment. Additionally, nanosphere lithography enables the surface density, size, and periodicity of the nanorings to be tuned by changing the diameters of silica microspheres and surface deposition time. Further, nanosphere lithography may be combined with surface chemistry such as siloxane reaction with hydroxyl to produced designed REN-organic composite materials. Finally, the combined capabilities are critical in characterizing structure in correlation with the upper conversion luminescent properties at single feature and single particle levels. These high-density, regular arrays of β-$NaYF_4$:Yb,Er nanorings inlaid in an OTS matrix demonstrate the feasibility of the production and size control of rare-earth-based nanostructures, which is a critical requirement in future device fabrication such as integration into photovoltaic cells or display monitors. This work lays the foundation for the construction of more complex structures such as multiple REN materials or 3D nanostructures.

MATERIALS AND METHODS

Materials. Octadecyltrichlorosilane (OTS) was purchased from Gelest (Morrisville, PA) and used without further purification. Chloroform (>99.8% purity), hydrogen peroxide (30% aqueous solution), sulfuric acid, and ammonium hydroxide were purchased from Fisher Scientific (Waltham, MA) and used as received. 18 MΩ water was generated from a Milli-Q system (Q-GARD 2, Millipore, Billerica, MA).

Substrate Preparation. Microscope coverslips (Fisher) with lateral dimensions of 220 mm^2 and thicknesses ranging from 0.13 to 0.17 mm were used as glass coverslips. Before use, the glass coverslips were immersed for 1 h in a piranha solution, which is a 3:1 mixture by volume of sulfuric acid and hydrogen peroxide. *Piranha is a vigorous oxidant and should be used with extreme caution!* The glass coverslips were then rinsed with copious amounts of 18 MΩ water and subsequently immersed into a base etch solution composed of a 5:1:1 mixture by volume of 18 MΩ water, ammonium hydroxide, and hydrogen peroxide. The glass jar with the glass coverslips and base etch solution was sealed and placed in an oven at 70 °C for 1 h. The glass coverslips were again rinsed with copious amounts of 18 MΩ water and then dried with nitrogen gas.

Silica Microsphere Preparation. An aliquot of a stock 1 μm silica sphere solution (8000 Series, Thermo Scientific, Waltham, MA) was pipetted into a microcentrifuge tube and subjected to centrifugation (model 5415c, eppendorf North America, Hauppauge, NY). The supernatant solution was removed, and the particle pellet at the bottom of a microcentrifuge tube was resuspended in 18 MΩ water using a vortex (Vortex-Genie 2, VWR, Randor, PA) to reach a concentration of 3% by weight. This centrifugation and suspension process was repeated 3 times before the microsphere suspension was used to generate the composite nanostructures.

β-$NaYF_4$:Yb,Er Nanocrystal Preparation and Characterization. Stock β-$NaYF_4$:Yb,Er nanocrystals were synthesized using previous oxygen free procedures.[39,40] An aliquot of stock β-$NaYF_4$:Yb,Er nanocrystal hexane solution was pipetted into a microcentrifuge tube, diluted with excess ethanol, and subjected to centrifugation. The supernatant solution was removed, and the nanocrystal pellet at the bottom of the microcentrifuge tube was suspended in chloroform to reach a concentration of 4 mg/mL. This centrifugation and resuspension process was repeated 3 times prior to solution deposition. The nanocrystal size and shape were determined using a transmission electron microscope (JEM-2100, JEOL, Japan) operated at 200 kV.

Home-Built Multilaser-line Atomic Force, Apertureless Near Field Scanning Optical, and Far-field Optical Microscopes. All AFM, NSOM, and far-field microscopy and spectroscopy data were acquired on the same home-built multifunctional instrument. An AFM instrument (MFP3D, Asylum Research, Santa Barbra, CA) was mounted above an inverted optical microscope (Olympus IX 50, Olympus America Inc., Melville, NY) with a PLAN APO 60× oil immersion microscope objective with an N.A. of 1.45 (Olympus America Inc.). The index matching immersion liquid with n = 1.5142 was purchased from Cargille Laboratories (Cedar Grove, NJ). A 405 nm, 10 mW thermoelectrically cooled diode laser (TECBL-10G-405, World Star Tech., Toronto, Canada) and a 980 nm, 50 mW diode laser (UH5-50G-980, World Star Tech.) were used as excitation sources for the Si_3N_4 tips and the β-$NaYF_4$:Yb,Er nanocrystals, respectively. These laser lines were combined using a 900dcsp-tan dichroic mirror (Chroma Technology Corporation, Bellows Falls, VT) and directed to the 60× objective using a 5 mm high index right angle prism (Olympus America Inc.). For NSOM imaging, a 430 nm long pass filter (HQ430LP, Chroma Technology Corporation) was used to remove the 405 nm excitation laser, a 785 nm short pass filter (SP01-785RU-25, Semrock Inc., Rochester, NY) was used to remove the AFM IR laser, and a 8 mm iris diaphragm (Linos Photonics, Milford, NJ) was used to eliminate stray and unfocused photons. For far-field microscopy and spectroscopy, a 750 nm short pass filter (ET750SP-2p, Chroma Technology Corporation) was used to remove the AFM IR laser and the 980 nm excitation laser. The luminescent light was collected by a photomultiplier tube (H5784-20, Hitachi, Pleasanton, CA) for NSOM imaging, by a CCD camera (Regtiga-2000R, QImaging, Surrey, Canada) for far-field microscopy, and by a fiber optical UV−vis spectrometer (USB 2000, Ocean Optics Inc., Dunedin, FL) for far-field spectroscopy.

Atomic Force Microscopy Imaging. Tapping mode AFM images were acquired with AC240 Si cantilevers (Olympus America Inc.) with force constants of 2 N/m. The drive frequency of the cantilever was offset at 5% lower than the cantilever resonance to gain stability and to maintain repulsive probe−surface interactions.[41,42] The damping of the amplitude was set at 40%, and scan rates were typically 0.6 Hz to maximize topographic tracking. Contact mode AFM and NSOM images were acquired with sharpened Si_3N_4 cantilevers (Veeco Metrology Group, Santa Barbra, CA) with force constants of 0.12 N/m. Typical image forces ranged from 5 to 15 nN, and scan rates were typically 0.8 Hz. AFM and NSOM image analysis was performed using the MFP3D's data and acquisition and analysis software package written on the Igor Pro platform (version 6.12a, Wavemetrics, Portland, OR). Far-field optical images were processed using ImageJ software (version 1.43u, National Institutes of Health, USA).

Acknowledgment. We thank Dr. Valentin Lulevich and Mr. Weifeng Lin at UC Davis for their helpful and insightful discussions. This work was supported the National Science Foundation (MRI-DMR-0723118, CMMI-0900644) and ACS-PRF-ND. This material is based, in part, upon work while serving at the National Science Foundation (by T.E.P.).

REFERENCES AND NOTES

1. Sandrock, T.; Scheife, H.; Heumann, E.; Huber, G. High-Power Continuous-Wave Upconversion Fiber Laser at Room Temperature. *Opt. Lett.* **1997**, *22*, 808–810.
2. Downing, E.; Hesselink, L.; Ralston, J.; Macfarlane, R. A Three-Color, Solid-State, Three-Dimensional Display. *Science* **1996**, *273*, 1185–1189.
3. Wang, Q. H.; Bass, M. Photo-Luminescent Screens for Optically Written Displays Based on Upconversion of near Infrared Light. *Electron. Lett.* **2004**, *40*, 987–989.
4. *Phosphor Handbook*; CRC Press: Boca Raton, FL, 1999.
5. Kim, W. J.; Nyk, M.; Prasad, P. N. Color-Coded Multilayer Photopatterned Microstructures Using Lanthanide (III) Ion Co-Doped $NaYF_4$ Nanoparticles with Upconversion Luminescence for Possible Applications in Security. *Nanotechnology* **2009**, *20*, 185301.
6. Ho, H. P.; Wong, W. W.; Wu, S. Y. Multilayer Optical Storage Disk Based on the Frequency up-Conversion Effect from Rare-Earth Ions. *Opt. Eng.* **2003**, *42*, 2349–2353.
7. Richards, B. S.; Shalav, A. The Role of Polymers in the Luminescence Conversion of Sunlight for Enhanced Solar Cell Performance. *Synth. Met.* **2005**, *154*, 61–64.
8. Shalav, A.; Richards, B. S.; Trupke, T.; Kramer, K. W.; Gudel, H. U. Application of $NaYF_4$: Er^{3+} up-Converting Phosphors for Enhanced near-Infrared Silicon Solar Cell Response. *Appl. Phys. Lett.* **2005**, *86*, 013505.
9. Shan, G. B.; Demopoulos, G. P. Near-Infrared Sunlight Harvesting in Dye-Sensitized Solar Cells *via* the Insertion of an Upconverter-TiO_2 Nanocomposite Layer. *Adv. Mater.* **2010**, *22*, 4373–4377.
10. Strumpel, C.; McCann, M.; Beaucarne, G.; Arkhipov, V.; Slaoui, A.; Svrcek, V.; del Canizo, C.; Tobias, I. Modifying the Solar Spectrum to Enhance Silicon Solar Cell Efficiency - an Overview of Available Materials. *Sol. Energy Mater. Sol. Cells* **2007**, *91*, 238–249.
11. Xiong, L. Q.; Chen, Z. G.; Tian, Q. W.; Cao, T. Y.; Xu, C. J.; Li, F. Y. High Contrast Upconversion Luminescence Targeted Imaging in Vivo Using Peptide-Labeled Nanophosphors. *Anal. Chem.* **2009**, *81*, 8687–8694.
12. Zhang, C.; Sun, L. D.; Zhang, Y. W.; Yan, C. H. Rare Earth Upconversion Nanophosphors: Synthesis, Functionalization and Application as Biolabels and Energy Transfer Donors. *J. Rare Earths* **2010**, *28*, 807–819.
13. van de Rijke, F.; Zijlmans, H.; Li, S.; Vail, T.; Raap, A. K.; Niedbala, R. S.; Tanke, H. J. Up-Converting Phosphor Reporters for Nucleic Acid Microarrays. *Nat. Biotechnol.* **2001**, *19*, 273–276.
14. Zhang, F.; Deng, Y. G.; Shi, Y. F.; Zhang, R. Y.; Zhao, D. Y. Photoluminescence Modification in Upconversion Rare-Earth Fluoride Nanocrystal Array Constructed Photonic Crystals. *J. Mater. Chem.* **2010**, *20*, 3895–3900.
15. Auzel, F. Upconversion and Anti-Stokes Processes with F and D Ions in Solids. *Chem. Rev.* **2004**, *104*, 139–173.
16. Shen, J.; Sun, L. D.; Yan, C. H. Luminescent Rare Earth Nanomaterials for Bioprobe Applications. *Dalton Trans.* **2008**, 5687–5697.
17. Binnemans, K. Lanthanide-Based Luminescent Hybrid Materials. *Chem. Rev.* **2009**, *109*, 4283–4374.
18. Huisman, C. L.; Schoonman, J.; Goossens, A. The Application of Inverse Titania Opals in Nanostructured Solar Cells. *Sol. Energy Mater. Sol. Cells* **2005**, *85*, 115–124.
19. Salafsky, J. S. A 'Channel' Design Using Single, Semiconductor Nanocrystals for Efficient (Opto)Electronic Devices. *Solid-State Electron.* **2001**, *45*, 53–58.
20. Xue, X. J.; Xu, W.; Wang, F.; Liu, X. G. Multiplex Single-Nucleotide Polymorphism Typing by Nanoparticle-Coupled DNA-Templated Reactions. *J. Am. Chem. Soc.* **2009**, *131*, 11668–11669.
21. Si, H. Y.; Yuan, D.; Chen, J. S.; Chow, G. M.; Zhang, H. L. Facile Patterning of Upconversion NaYF4:Yb, Er Nanoparticles. *J. Colloid Interface Sci.* **2011**, *353*, 569–573.
22. Kim, E.; Xia, Y. N.; Whitesides, G. M. Two- and Three-Dimensional Crystallization of Polymeric Microspheres by Micromolding in Capillaries. *Adv. Mater.* **1996**, *8*, 245–247.
23. Kim, E.; Xia, Y. N.; Whitesides, G. M. Polymer Microstructures Formed by Molding in Capillaries. *Nature* **1995**, *376*, 581–584.
24. Yan, C.; Dadvand, A.; Rosei, F.; Perepichka, D. F. Near-Ir Photoresponse in New up-Converting CdSe/$NaYF_4$:Yb,Er Nanoheterostructures. *J. Am. Chem. Soc.* **2010**, *132*, 8868–8869.
25. Bao, Y.; Luu, Q. A. N.; Lin, C. K.; Schloss, J. M.; May, P. S.; Jiang, C. Y. Layer-by-Layer Assembly of Freestanding Thin Films with Homogeneously Distributed Upconversion Nanocrystals. *J. Mater. Chem.* **2010**, *20*, 8356–8361.
26. Tan, M. C.; Patil, S. D.; Riman, R. E. Transparent Infrared-Emitting CeF_3:Yb-Er Polymer Nanocomposites for Optical Applications. *ACS Appl. Mater.* **2010**, *2*, 1884–1891.
27. Jarai-Szabo, F.; Astilean, S.; Neda, Z. Understanding Self-Assembled Nanosphere Patterns. *Chem. Phys. Lett.* **2005**, *408*, 241–246.
28. Kondo, M.; Shinozaki, K.; Bergstrom, L.; Mizutani, N. Preparation of Colloidal Monolayers of Alkoxylated Silica Particles at the Air-Liquid Interface. *Langmuir* **1995**, *11*, 394–397.
29. Dimitrov, A. S.; Nagayama, K. Continuous Convective Assembling of Fine Particles into Two-Dimensional Arrays on Solid Surfaces. *Langmuir* **1996**, *12*, 1303–1311.
30. Kralchevsky, P. A.; Denkov, N. D. Capillary Forces and Structuring in Layers of Colloid Particles. *Curr. Opin. Colloid Interface Sci.* **2001**, *6*, 383–401.
31. Li, J. R.; Garno, J. C. Elucidating the Role of Surface Hydrolysis in Preparing Organosilane Nanostructures via Particle Lithography. *Nano Lett.* **2008**, *8*, 1916–1922.
32. Li, J. R.; Yin, N. N.; Liu, G. Y. Hierarchical Micro- and Nanoscale Structures on Surfaces Produced Using a One-Step Pattern Transfer Process. *J. Phys. Chem. Lett.* **2011**, *2*, 289–294.
33. Chen, J. X.; Liao, W. S.; Chen, X.; Yang, T. L.; Wark, S. E.; Son, D. H.; Batteas, J. D.; Cremer, P. S. Evaporation-Induced Assembly of Quantum Dots into Nanorings. *ACS Nano* **2009**, *3*, 173–180.
34. Lulevich, V.; Ducker, W. A. Scanning near-Field Optical Microscopy Utilizing Silicon Nitride Probe Photoluminescence. *Appl. Phys. Lett.* **2005**, *87*, 214107.
35. Lulevich, V.; Honig, C.; Ducker, W. A. An Atomic Force Microscope Tip as a Light Source. *Rev. Sci. Instrum.* **2005**, *76*, 123704.
36. Schietinger, S.; Menezes, L. D.; Lauritzen, B.; Benson, O. Observation of Size Dependence in Multicolor Upconversion in Single Yb^{3+}, Er^{3+} Codoped $NaYF_4$ Nanocrystals. *Nano Lett.* **2009**, *9*, 2477–2481.
37. Suyver, J. F.; Aebischer, A.; Biner, D.; Gerner, P.; Grimm, J.; Heer, S.; Kramer, K. W.; Reinhard, C.; Gudel, H. U. Novel Materials Doped with Trivalent Lanthanides and Transition Metal Ions Showing near-Infrared to Visible Photon Upconversion. *Opt. Mater.* **2005**, *27*, 1111–1130.
38. Mai, H. X.; Zhang, Y. W.; Sun, L. D.; Yan, C. H. Highly Efficient Multicolor up-Conversion Emissions and Their Mechanisms of Monodisperse $NaYF_4$: Yb,Er Core and Core/Shell-Structured Nanocrystals. *J. Phys. Chem. C* **2007**, *111*, 13721–13729.
39. Mai, H. X.; Zhang, Y. W.; Si, R.; Yan, Z. G.; Sun, L. D.; You, L. P.; Yan, C. H. High-Quality Sodium Rare-Earth Fluoride Nanocrystals: Controlled Synthesis and Optical Properties. *J. Am. Chem. Soc.* **2006**, *128*, 6426–6436.
40. Sun, X.; Zhang, Y. W.; Du, Y. P.; Yan, Z. G.; Si, R.; You, L. P.; Yan, C. H. From Trifluoroacetate Complex Precursors to Monodisperse Rare-Earth Fluoride and Oxyfluoride Nanocrystals with Diverse Shapes through Controlled Fluorination in Solution Phase. *Chem.—Eur. J.* **2007**, *13*, 2320–2332.
41. Garcia, R.; Perez, R. Dynamic Atomic Force Microscopy Methods. *Surf. Sci. Rep.* **2002**, *47*, 197–301.
42. Weisenhorn, A. L.; Maivald, P.; Butt, H. J.; Hansma, P. K. Measuring Adhesion, Attraction, and Repulsion between Surfaces in Liquids with an Atomic-Force Microscope. *Phys. Rev. B.* **1992**, *45*, 11226–11232.